Layered Double Hydroxide-Based Gas Sensors for VOC Detection at Room Temperature

ACS OMEGA

http://pubs.acs.org/journal/acsodf

Article

Layered Double Hydroxide-Based Gas Sensors for VOC Detection at Room Temperature

Lorenzo Vigna, Arianna Nigro, Alessio Verna, Ivan Vito Ferrari, Simone Luigi Marasso,* Sergio Bocchini, Marco Fontana, Angelica Chiodoni, Candido Fabrizio Pirri, and Matteo Cocuzza

Cite This: *ACS Omega* 2021, 6, 20205−20217

Read Online

ACCESS | Metrics & More | Article Recommendations | Supporting Information

ABSTRACT: Miniaturized low-cost sensors for volatile organic compounds (VOCs) have the potentiality to become a fundamental tool for indoor and outdoor air quality monitoring, to significantly improve everyday life. Layered double hydroxides (LDHs) belong to the class of anionic clays and are largely employed for NO_x detection, while few results are reported on VOCs. In this work, a novel LDH coprecipitation method is proposed. For the first time, a study comparing four LDHs (ZnAl−Cl, ZnFe−Cl, ZnAl−NO_3, and MgAl−NO_3) is carried out to investigate the sensing performances. As explored through several microscopy and spectroscopy analyses, LDHs show a morphology characterized by a large surface area and a three-dimensional hierarchical flowerlike architecture with micro- and nanopores that induce a fast diffusion and highly effective surface interaction of the target gases. The fabricated sensors, operating at room temperature, are able to reversibly and selectively detect acetone, ethanol, ammonia, and chlorine vapors, reaching significant sensing response values up to 6% at 21 °C. The results demonstrate that by changing the LDHs' composition, it is possible to modulate the sensitivity and selectivity of the sensor, helping the discrimination of different analytes, and the consequent integration on a sensor array paves the way for electronic nose development.

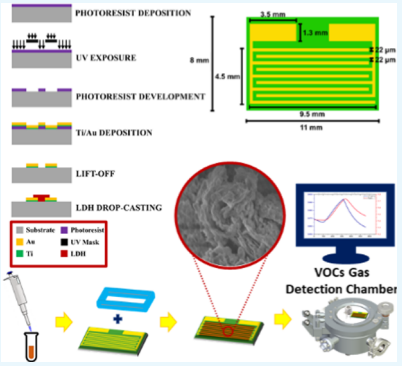

1. INTRODUCTION

Natural formation of layered double hydroxide (LDH) minerals was discovered by Hochstetter et al. 18 decades ago,[1] but only 100 years later Feitknecht et al. and other researchers were able to synthesize them.[2−9] Since then LDHs have garnered enormous interest on the scientific scene due to their unique tailoring properties and simple synthesis, which make them suitable for a variety of different applications. LDHs are two dimensional (2D) ionic lamellar materials belonging to the class of anionic clays.[10] Also widely known as hydrotalcite-like compounds due to their molecular structures, LDHs are characterized by a lattice, which is constituted by the stacking of charged brucite-shaped layers made of divalent metal ions M^{2+} (e.g., Ca^{2+}, Zn^{2+}, Mg^{2+}, Co^{2+}, and Ni^{2+}) occupying the centers of edge-sharing octahedra, surrounded by six OH^- hydroxyl groups.[11−13] Some of the divalent cations are substituted by trivalent metal ions M^{3+} (e.g., Al^{3+}, Fe^{3+}, Cr^{3+}, Ga^{3+}, and In^{3+}), leading to the formation of positively charged lamellas. To maintain the global electrostatic neutrality, the positive charge sheets need to be balanced by the presence of exchangeable anions A^{n-} (e.g., CO_3^{2-}, Cl^-, SO_4^{2-}, OH^-, and NO_3^-) located in the interlayer spaces along with water molecules, which establish a network of hydrogen bonds providing additional active sites for external molecules.[11] Synthetically, the chemical structure may be written as (eq 1)

$$[M^{2+}_{1-x}\, M^{3+}_{x}\, (OH)_2]_2 \cdot [A_{x/n}]^{n-} \cdot mH_2O \quad (1)$$

These materials possess interesting physical and chemical properties related to those of clays due to their unique structural amenability and high compositional flexibility. What makes them of paramount importance is the great number of possible chemical compositions that can be synthesized by slightly changing the nature of the two cations and their molar ratios and by freely inserting different molecular anions in the interlayer spacing. In general, LDHs display a large specific surface area, good electrical conductivity, high stability and permeability, anion exchangeability, biocompatibility, low cost, and excellent processability.[14−18] Accordingly, the aforementioned properties have increased their popularity in many different research fields and applications ranging from electrochemistry,[19] biosensors,[5,20,21] and photochemistry[22] to catalysis,[23,24] medicine as drug delivery media,[25−27] analytical chemistry as adsorbents for wastewater treatment,[14,28] and environmental monitoring for the development of electronic

Received: April 16, 2021
Accepted: July 14, 2021
Published: July 29, 2021

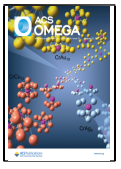

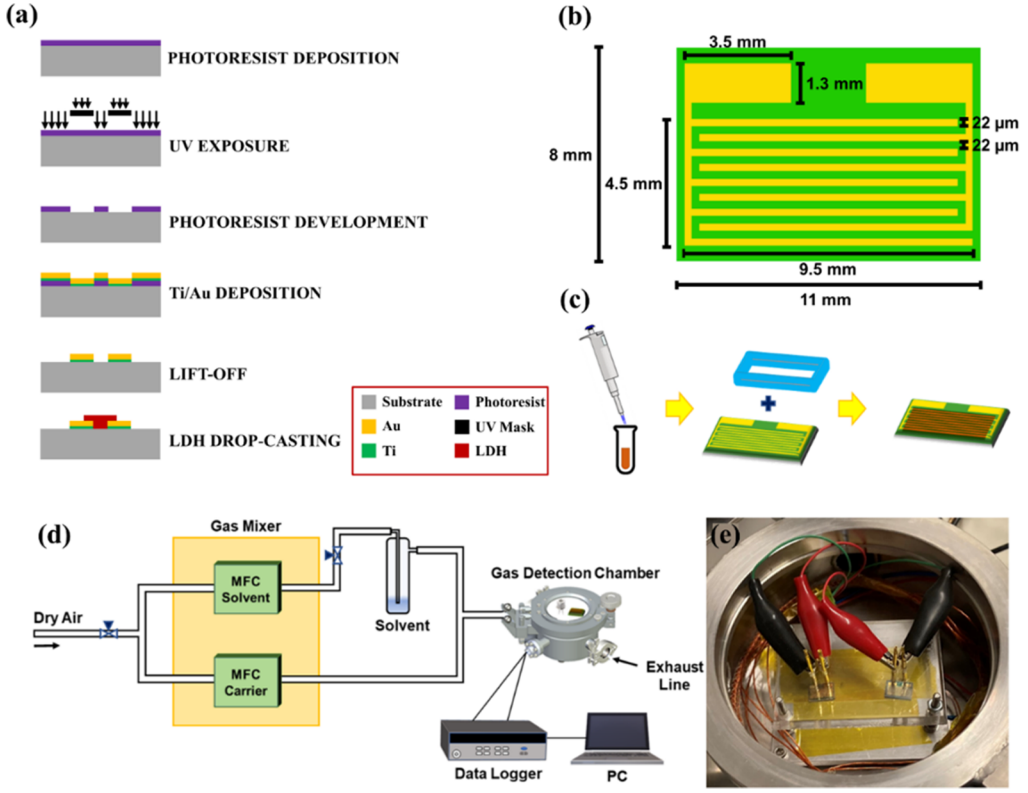

Figure 1. (a) Sketch of the fabrication steps used to produce LDH gas sensors. (b) Layout of the device with contact pads and interdigitated electrodes. (c) Fabrication of the device through a drop-cast technique with the help of a PDMS mold, (d) Scheme of the experimental sensing setup used to perform real-time gas-sensing measurements. (e) Interior of the gas detection chamber.

noses.[29,30] In this framework, currently, with the development of industry and technology, environmental pollution has become a global issue and the demand for air quality control is becoming increasingly important. Among all of the contaminants in air, volatile organic compounds (VOCs) such as acetone, ethanol, and ammonia vapors are the most common and hazardous. Even at very low concentrations these molecules not only pollute the environment, but also directly affect human health and climate change.[18,31,32] Commercial gas sensors are based on different transduction mechanisms and materials, which include polymers,[33−36] metal oxides,[37−39] or nanocomposites.[16,17,40−48] The most common are the ones based on metal oxide semiconductors, which require high working temperatures to obtain good sensitivities, fast response, and selectivity.[39,49,50] Morandi et al. fabricated a CH_4 sensor using Pt/Zn/Al-LDH operating at 450 °C.[37] This entails an increase in power consumption and device complexities, and it is unfavorable for device stability and flammable or explosive environments. For this reason, research activities are concentrated toward the development of new gas sensors that operate at room temperature and are able to ensure an accurate, reliable, and fast response for human health protection and air quality monitoring. Within this context, to the best of our knowledge, LDHs have been successfully used as chemiresistive gas sensors especially for the detection of NO_x,[17,18,42−44,47,50−54] but most of them are insensitive to VOCs.[17,18,42,43,46,48,53,54] Therefore, the possibility of employing miniaturized sensors based on LDHs for the detection of traces of VOCs represents a great advantage in many aspects, owing to their versatility in both chemical composition and structural morphology. In addition, the high porosity allows LDHs to show adjustable interlayer gallery pathways for atoms and molecules, enabling a fast diffusion and carrier transportation through the entire particle bulk[45] and, at the same time, the short-range order allows a fast hole-trapping process where electrons can transfer within unit sheets freely and sufficiently until reaching the sheet edges, improving sensitivity, selectivity, stability, response, and recovery time.[50]

The present work aims to provide an accurate investigation of the gas-sensing behaviors of these materials. To this end, among all LDH systems, four different compositions ZnAl−Cl, ZnFe−Cl, ZnAl−NO_3, and MgAl−NO_3 were synthesized via a simple coprecipitation method in aqueous solution and four different types of resistive gas sensors were fabricated by cleanroom technologies and drop casting (Figure 1a−c). The different LDHs were investigated through field emission scanning electron microscopy (FESEM), Fourier transform infrared spectroscopy (FTIR), X-ray photoelectron spectroscopy (XPS), energy-dispersive X-ray analysis (EDX), and X-ray diffraction (XRD). Finally, the sensing response at room temperature toward a low concentration range of four different VOC vapors up to 10% of the saturated vapor pressure was evaluated by acquiring the real-time variation of the electrical resistance as a function of time by means of a proper characterization system (Figure 1d,e). The selected compositions were chosen since a comparison between LDHs with a wide variety of metal ions and intercalated anions allows investigation of sensing properties in view of selectivity tunability. The obtained results provide a wide range of potentialities to be explored related to the sensing performances and show that this class of materials is able to detect and discriminate the target gases at different concentrations at

https://doi.org/10.1021/acsomega.1c02038
ACS Omega 2021, 6, 20205−20217

room temperature, paving the way for the electronic nose system development for monitoring air pollution.

2. RESULTS AND DISCUSSION

Due to the high compositional flexibility and unique molecular structure, LDHs are excellent candidates for gas sensing. For this reason, a good understanding of material properties and the sensing mechanism are of crucial importance for the optimization of LDH devices and they should be investigated from the atomistic point of view all the way to their macroscopic dimensions. The electrical conductivity shows an anisotropic behavior due to the alignment and arrangement of the lamellas in the 2D geometry. All of the deposited thin films display an electrical resistance used as the baseline value in the range of hundreds of ohms revealing a good charge-carrier mobility and carrier density, especially along the longitudinal lamellae's axis, making them suitable for the active layer in electronic devices. Furthermore, all of the films showed good stability concerning the conductivity. Indeed, no appreciable variations were observed after 6 months.

The crystal structure was investigated by X-ray powder diffraction. All of the XRD patterns are provided in Figure 2, alongside a simulated pattern for ZnAl−NO_3 obtained from the structural model published in ref 59.

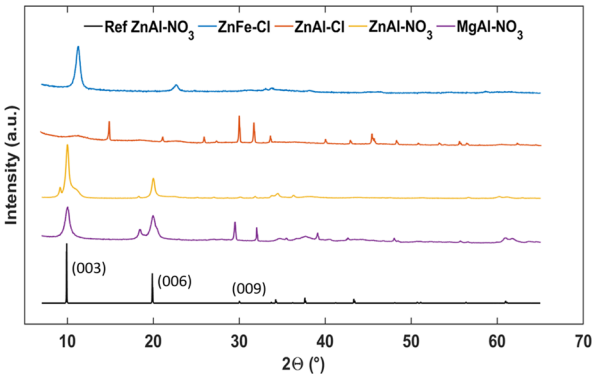

Figure 2. XRD patterns of samples ZnAl−Cl, ZnFe−Cl, ZnAl−NO_3, MgAl−NO_3, and the reference pattern for ZnAl−NO_3.[59]

They confirm the presence of a typical hydrotalcite-like structure exhibiting a peak corresponding to the (00λ) crystal plane of the LDH. Regarding ZnFe−Cl and ZnAl−NO_3, the patterns can be described with a hexagonal cell with $R\bar{3}m$ space group symmetry, with the following cell parameters

$$-\mathrm{ZnFe} - \mathrm{Cl}: a = 3.098\ \text{Å}, c = 23.442\ \text{Å}$$

$$-\mathrm{ZnAl} - \mathrm{NO_3}: \mathrm{a} = 3.082\ \text{Å}, \mathrm{c} = 26.824\ \text{Å}$$

which correspond to the (003) d-spacing values of 7.81 and 8.94 Å, respectively. These results are in accordance with LDH structures previously reported in the literature.[4,59,60]

Regarding sample MgAl−NO_3, the peaks corresponding to the (003) and (006) families of crystallographic planes are clearly identified, allowing for the calculation of a corresponding d-spacing of 8.81 Å. However, it was not possible to ascribe the complete set of peaks to a single crystalline phase.

Regarding sample ZnAl−Cl, the XRD spectrum is quite different with respect to the other samples, with many reflections corresponding to non-LDH phases. Specifically, it is possible to identify a contribution from halite (NaCl, Crystallography Open Database ID:2108652) with (111), (200), and (220) peaks at about 27.6, 31.9, and 45.8° in 2θ, respectively. However, it must be stressed that broad peaks are present at 2θ values typical of the (003) and (006) crystallographic planes of the LDH structure, suggesting that in this sample the crystalline order along the c-stacking direction extends over a few layers only. This is corroborated by the application of the Scherrer equation to the (003) peak for the different samples (Table 1), with the ZnAl−Cl sample exhibiting a coherent scattering domain significantly smaller than the other samples. It must be stressed that the reported values must be intended as lower bounds to the size of the coherent scattering domain along the c-stacking direction, since the contribution to peak broadening due to the diffractometer was not taken into account.

Table 1. Analysis of the (003) Peak from XRD Patterns of Different LDH Samples

sample	2θ	d(003) (Å)	size (nm)
ZnAl−Cl	11.199	7.79	4
ZnFe−Cl	11.320	7.81	12
ZnAl−NO_3	9.886	8.94	15
MgAl−NO_3	10.027	8.81	11

The morphology of the LDH structures after the deposition over the electrodes was investigated through a FESEM analysis. The detailed microstructures show a high degree of difference based on the synthesis process and the molar ratio M^{2+}/M^{3+}. In general, according to the literature,[18,44,47,51−53] the best performance in gas-sensing applications is achieved when the structure assumes a typical porous hierarchical 3D flowerlike arrangement like the one shown in Figure 3a, where the microstructure of ZnFe−Cl with a Zn/Fe molar ratio of 1.3 is represented. In addition, it is possible to notice many coarse interspaces between the layered nanopetals, confirming the presence of mesopores allowing the exposure of more active sites of the internal surface area for the interactions with the targeted gas molecules. For this reason, to ensure this structure, the best molar ratio M^{2+}/M^{3+} has been chosen during the synthesis process. If the molar ratio is too low, the structure is characterized by thick and irregular sheets with a heavy stack induced by the high density of layer charge. Otherwise, if the molar ratio is too high, the low substitution of M^{3+} in the $M^{2+}(OH)_2$ layers induces the formation of LDHs with a highly reduced porosity (Figure 3b). Only when the molar ratio is set to its optimum value, a structure with a perfect hierarchical flowerlike morphology is obtained. Generally, the crystal growth process in an aqueous phase system is characterized by a nucleation step and a growth stage. In this case, during the synthesis process, LDH crystal nuclei are formed and they crystallize in brucite-like layers where the trivalent cations partially replace the bivalent ones in the right proportion, inducing a specific positive charge. At this point, to minimize the overall surface energy, the grown ultrathin layered nanosheets tend to self-assemble uniformly and connect each other via edge amalgamation to form a stable and ordered flowerlike architecture with a high porosity.[17,52] A further comment can be provided regarding ZnAl−Cl and ZnAl−NO_3 LDHs. Of the two samples, the Al amount was found to be higher for ZnAl−NO_3. This result can be correlated with the morphology of the material, since a larger M^{3+} content leads to smaller nanosheet aggregates.[45,61] In

https://doi.org/10.1021/acsomega.1c02038
ACS Omega 2021, 6, 20205−20217

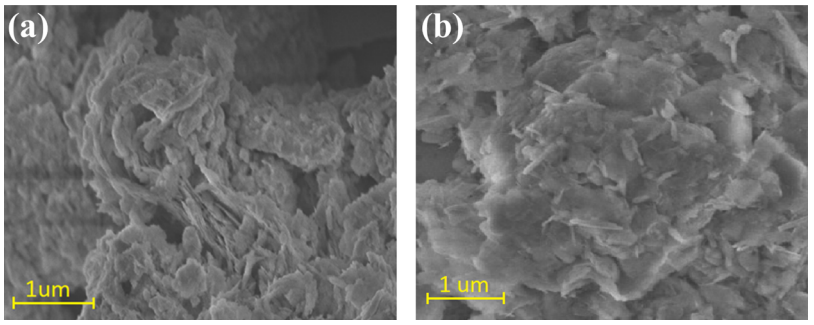

Figure 3. FESEM top view images of (a) flowerlike ZnFe−Cl with a Zn/Fe molar ratio of 1.3 and (b) ZnAl−NO_3 with a Zn/Al molar ratio of 2.2.

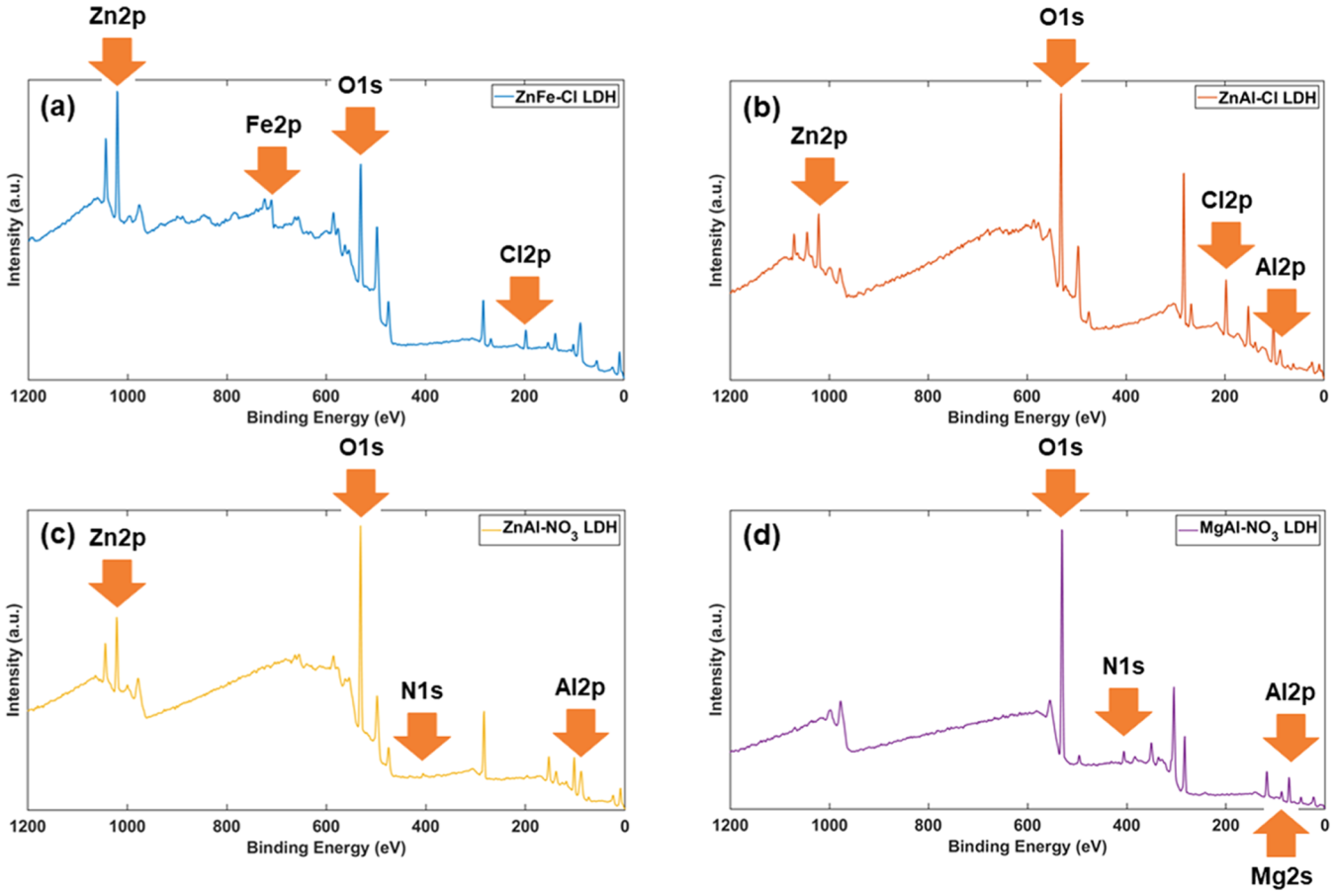

Figure 4. XPS survey spectra of (a) ZnFe−Cl, (b) ZnAl−Cl, (c) ZnAl−NO_3, and (d) MgAl−NO_3.

general, the size is related to nucleation and growth rates, since as the former increases and the latter decreases the size of grains gets smaller and vice versa. A high Al content leads to an increase in the number of available nucleation sites, therefore implying a high nucleation rate and smaller grain sizes. Typical of layered categories, these structures allow the formation of gallery pathways, resulting in an easy transportation of the analyte and allowing for its adsorption not only on the outer surfaces but also throughout the entire particle bulk, together with a high surface area and good permeability, strongly influenced by a high porosity.[44] These features appear to be beneficial in gas-sensing applications to improve the response time, compared with polycrystalline metal oxide sensors, whose charge carriers need to overcome the energy barrier formed at the interface of adjacent grains by thermionic emission to maintain their movement from one grain to the neighboring one.

XPS characterization has been performed on the four samples for each LDH composition to evaluate the elemental surface analysis of the material. In Figure 4 is shown the survey spectra where all of the main peaks related to the two metal cations, the oxygen species, and the interlayer anions are highlighted.

In all of the samples, it is possible to observe the O 1s peak at the binding energy (BE) around 530 eV. As detailed in Table 4, it represents the predominant atomic percentage and it is of a great relevance because it can show the excess concentration of chemisorbed oxygen that is strictly related to the sensing mechanism hence affecting the sensing response and boosting the charge transfer. In fact, the O 1s can be convoluted into three peaks by applying a Gaussian−

https://doi.org/10.1021/acsomega.1c02038
ACS Omega 2021, 6, 20205−20217

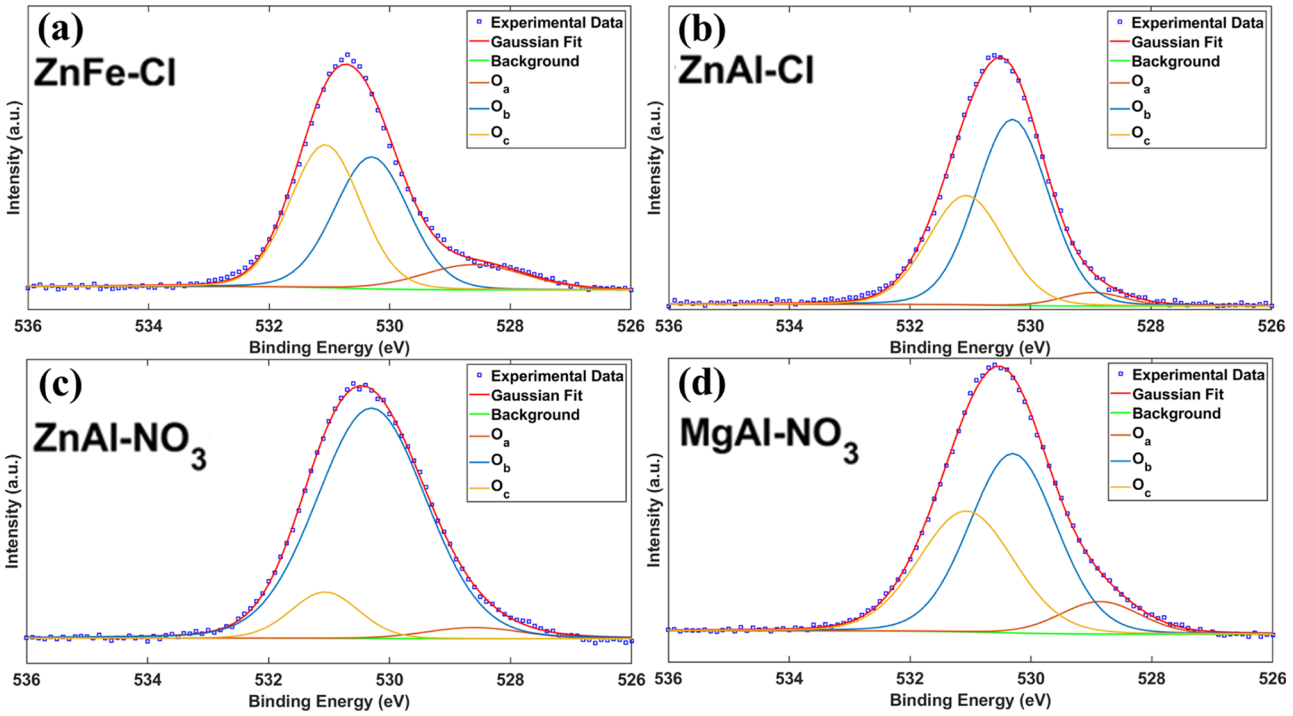

Figure 5. XPS high-resolution O 1s spectra of (a) ZnFe−Cl, (b) ZnAl−Cl, (c) ZnAl−NO_3, and (d) MgAl−NO_3.

Lorentzian fitting, corresponding to three different oxygen species on the surface of the material (Figure 5). The first one (O_a ∼ 529.4 eV) belongs to the lattice oxygen; the peak around 531.7 eV (O_c) is associated with chemisorbed and dissociated oxygen belonging to a specific species such as adsorbed water molecules or adsorbed O_2, while the last one, centered at 530.8 eV (O_b), is associated with O_2^- ions that are in oxygen deficient/vacancy structure regions.[18,53] The more chemisorbed oxygen species, the more possibility of interaction with the VOC molecules, resulting in a significant change in electrical resistance, affecting the sensing response.

A second peak common to all of the samples is located at BE around 289 eV, and it corresponds to C 1s, also referred to as adventitious carbon, which is nearly always present in XPS spectra since introduced on samples by the laboratory environment. Considering the main chemical constituents of the four samples, it is possible to notice that Zn 2p and Al 2p are correctly located at a BE of 1022 eV and BE of 75.9 eV, corresponding to Zn^{2+} and Al^{3+} oxidation states. The same considerations apply to Mg 2s and Fe 2p, showing peaks at a BE of 89 eV and BE of 707 eV, respectively. As regards the interlayer anions, Cl 2p and N 1s peaks can be observed at BE around 198 eV and a BE of 407 eV. They refer to the presence of Cl^- and NO_3^- species as intercalated anions. Table 2 summarizes the location of the main peaks for each element together with their atomic percentage. From these data, it is therefore possible to estimate the atomic ratio M^{2+}/M^{3+} for the four compositions. These results confirm the considerations mentioned regarding the morphology of the samples: the petal size gets smaller when increasing the amount of Al.

EDX is performed as a complementary analysis to the XPS survey to provide a further estimation of the elemental composition of the active layer and, in this way, verify the presence of the intercalated anions. According to Figure 6, it is possible to observe that the main peaks of the analyzed materials correctly correspond to the chemical elements highlighted before, confirming that the structures are composed of the expected metal constituents Zn, Al, Fe, and Mg, by the lattice oxygen and that the two anions, Cl^- and NO_3^-, were correctly intercalated between the metallic layers. The other peaks can be ignored since they correspond to Au and Si, coming from the electrodes and the underlying SiO_2 insulating layer, respectively.

Table 2. XPS Quantitative Results of the Four Compositions Analyzed with M^{2+}/M^{3+} Molar Ratios

compositions	peak	BE (eV)	atomic (%)	M^{2+}/M^{3+}
ZnFe−Cl	Zn $2p_{3/2}$	1022	9.1	1.3
	Fe $2p_{3/2}$	89	7.2	
	Cl 2p	198	4.1	
	O 1s	530	41.0	
	C 1s	289	34.1	
ZnAl−Cl	Zn $2p_{3/2}$	1022	1.8	1.5
	Al 2p	75.9	1.2	
	Cl 2p	198	5.4	
	O 1s	530	27.1	
	C 1s	289	49.4	
ZnAl−NO_3	Zn $2p_{3/2}$	1022	3.8	2.2
	Al 2p	75.9	1.7	
	N 1s	407	1.0	
	O 1s	530	44.7	
	C 1s	289	35.0	
MgAl−NO_3	Mg 2s	89	5.7	0.5
	Al 2p	75.9	11.5	
	N 1s	407	3.5	
	O 1s	530	49.5	
	C 1s	289	26.9	

FTIR spectroscopy in ATR mode was undertaken to explore the chemical environment of LDH powders (Figure 7). Although all samples showed rather similar spectra, subtle differences could still be noted because of the different cations

https://doi.org/10.1021/acsomega.1c02038
ACS Omega 2021, 6, 20205−20217

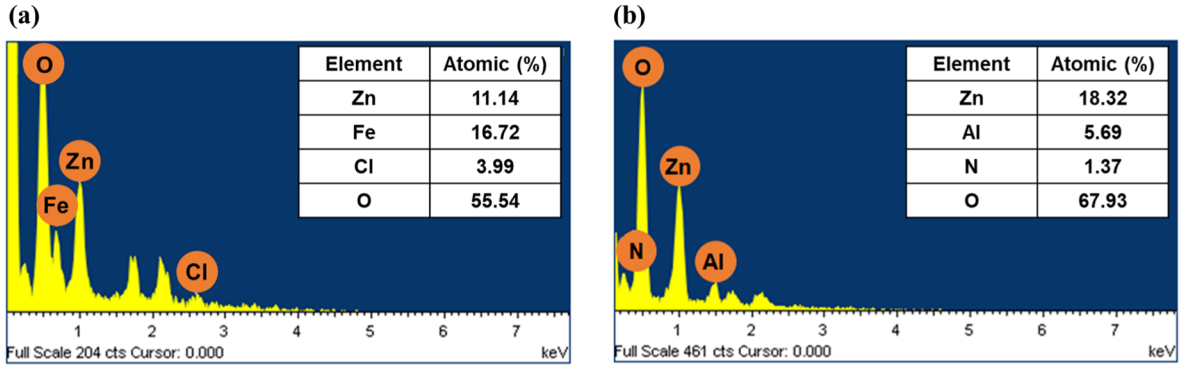

Figure 6. EDX spectra of LDH (a) ZnFe−Cl and (b) ZnAl−NO_3 surfaces.

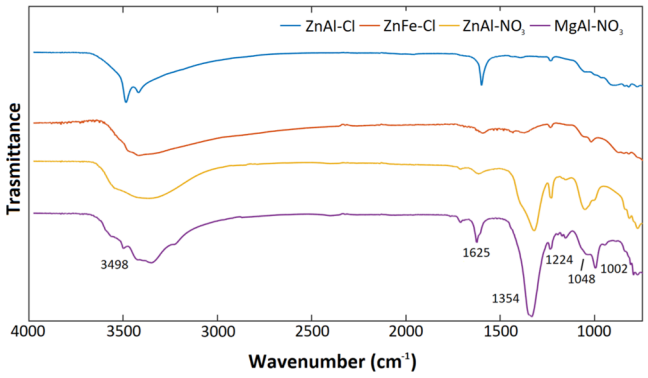

Figure 7. ATR−FTIR spectra of ZnFe−Cl, ZnAl−Cl, ZnAl−NO_3, and MgAl−NO_3.

and intercalated anions present in the various synthesized compositions.

The main characteristic LDH peaks were identified for the four different compositions since they share the overall analogous structure. According to the literature,[15,47,50,51] all of the spectra present a narrow absorption peak located at around 3500 cm^{-1} and a broad one at 3440 cm^{-1} corresponding to the stretching vibrations of the surface −OH groups in the brucite-like layers and of the hydrogen-bonded water molecules located in the interlayer space. The weaker peak at 1625 cm^{-1} is instead attributed to the interlamellar water bending.[62] The strong band at 1354 cm^{-1} in the ZnAl−NO_3 and MgAl−NO_3 are instead due to the antisymmetric stretching vibrations of N−O in NO_3, confirming its intercalation into LDHs, consistent with the XPS results. Peaks in the low-frequency region (800−400 cm^{-1}) ascribed to the vibrations of M−O, O−M−O, and M−O−M groups should complete the spectra, but they could not be detected because of the high background due to the total reflectance technique adopted.

In this work, four sets of devices described in the aforementioned section, one for each synthesized composition, were selected to be tested in their sensing behavior as chemiresistors toward four different analytes at room temperature, following the protocol reported in the experimental part. Four vapors were investigated starting from the liquid solvent, including one ketone (acetone), one alcohol (EtOH), a common bleach based on NaClO, and NH_3 molecules from NH_4OH liquid solution. These VOCs were selected because of their different chemical and physical properties such as functional groups. The gas concentrations for real-time exposure are reported as the percentage with respect to the saturation vapor pressures. Figure 8 displays a typical dynamic

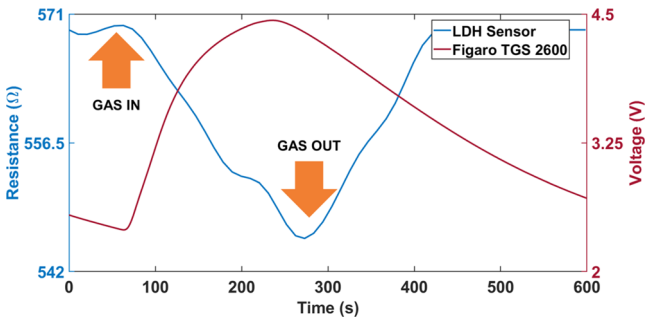

Figure 8. Example of a real-time sensing measurement of ZnFe−Cl toward 10% of EtOH along with the commercial Figaro TGS 2600 response.

sensing curve, where the electrical resistance is expressed as a function of time and the dark red curve is related to a commercial sensor that has been used as a reference.

Noticeably, all of the tested sensors were correctly able to detect at least one of the four considered analytes, and their sensing responses varied according to the specific chemical composition of the active layer. From the real-time response it is possible to state that as the reducing gas is fluxed in the detection chamber, the sensors respond to its presence with a constantly rapid decrease in the electrical resistance values of their sensing element, up to a saturation point. A complete recovery of the initial baseline value is quickly achieved by removing the analyte through a continuous flux of dry air. The drift of the resistance is almost negligible and all of the times the sensor recovered to the original value of the steady-state baseline as the sensing mechanism is a reversible process. As expected, the sensing response increased as the gas concentration in the chamber went up (Figure 9). According to the performed tests, ZnAl−Cl and ZnAl−NO_3 sensors only detected NH_3 vapors, achieving maximum sensitivity values of 3.8 and 5%, respectively. This was mainly due to the improved reaction between NH_3 and the absorbed oxygen (O_2^-). The difference can be explained on the basis of two factors: (1) as evidenced from FESEM and XPS analysis, the latter possesses a higher Al (M^{3+}) content, which results in the formation of smaller nanosheet aggregates favoring gas diffusion throughout the material and (2) the intercalation of NO_3 anions instead of Cl ones induces an increase in the interlayer distance between successive cationic layers, resulting in larger pathway galleries for the transportation of the gas as highlighted in the XRD

https://doi.org/10.1021/acsomega.1c02038
ACS Omega 2021, 6, 20205−20217

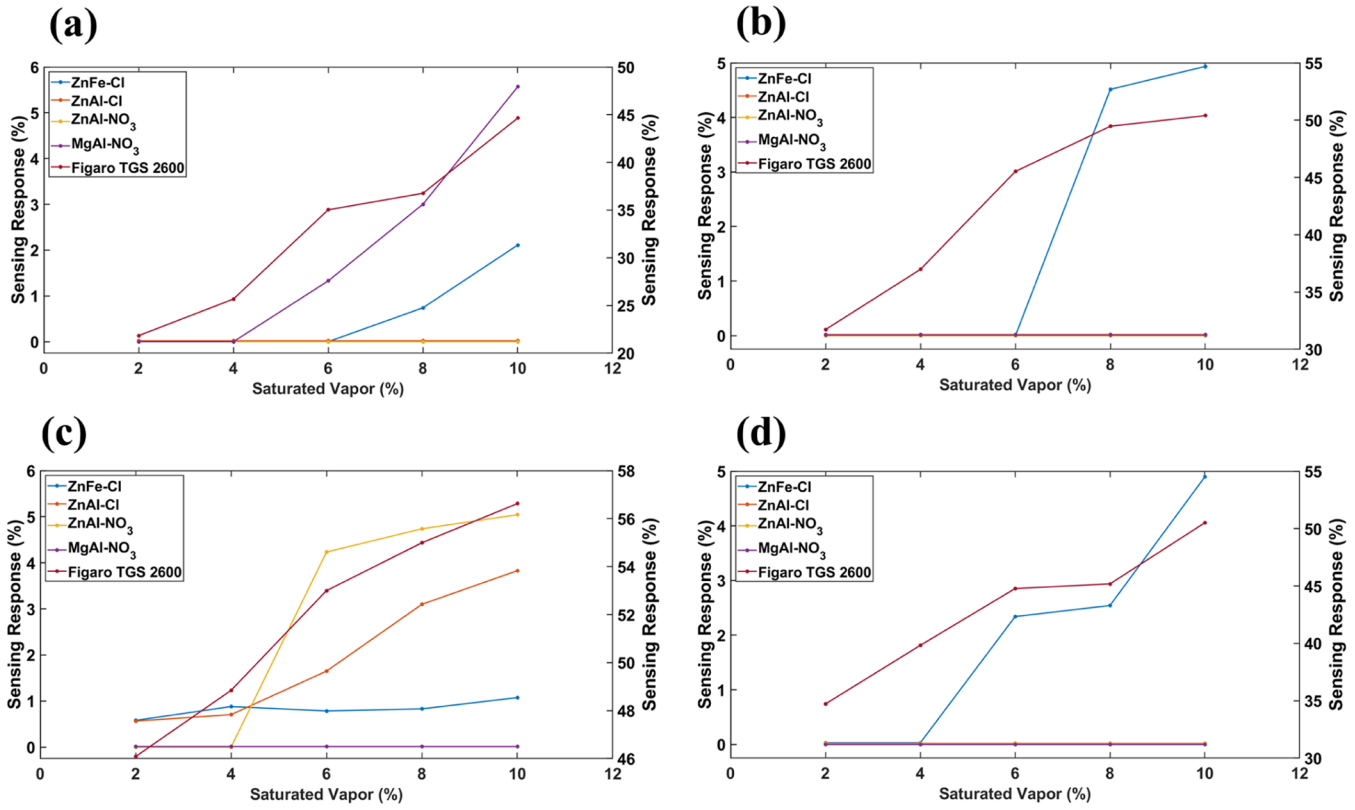

Figure 9. Gas-sensing response as a function of gas content for the different LDH sensors at room temperature and the commercial Figaro (right axis) toward (a) acetone, (b) EtOH, (c) NH_3, and (d) Cl vapors. The analyte concentration is reported as the percentage of their saturated partial vapor pressure.

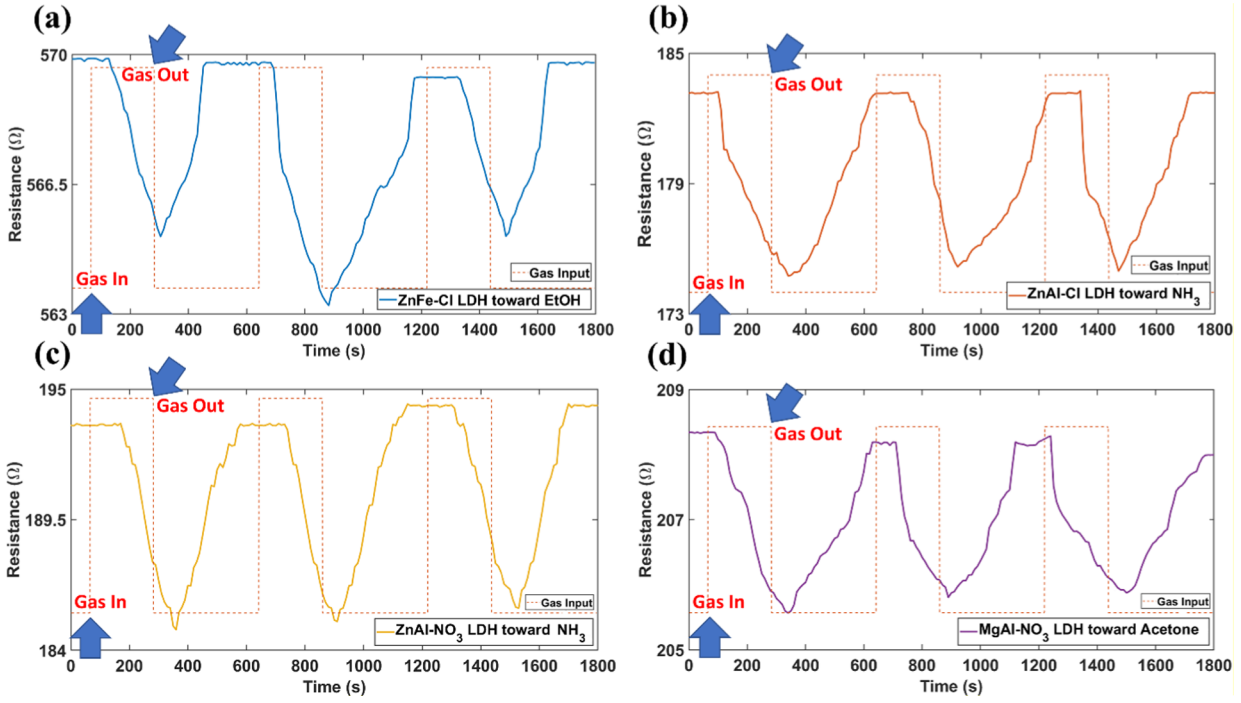

Figure 10. Three cycle real-time sensing measurements of (a) ZnFe−Cl, (b) ZnAl−Cl, (c) ZnAl−NO_3, and (d) MgAl−NO_3 toward ethanol, ammonia, and acetone vapors at a fixed concentration of 10% of saturated vapor at room temperature. Dotted lines represent the analyte's presence or absence in the sensing chamber.

analysis. The ZnFe−Cl sensor successfully detected all of the four tested analytes, achieving the highest sensitivity values for ethanol and chlorine vapors (~4.9%). The MgAl−NO_3 sensor was instead able to detect acetone vapors, with maximum sensitivity values of 5.6%. ZnAl−Cl and ZnFe−Cl sensors managed a detection of analytes at concentrations as low as

https://doi.org/10.1021/acsomega.1c02038
ACS Omega 2021, 6, 20205−20217

2%, while for the others the minimum achieved threshold was 6% of the saturated vapor pressure. The sensing response toward lower concentrations could not be distinguished clearly from the measurement's nose.

As regards the response and recovery times, with the increase of concentration, the response time is shortened but larger is the time required to recover after the gas is removed. In more detail, both ZnAl-based sensors were the slowest in responding and in recovering in the presence of the analytes. Finally, as is shown in Figure 10, the repeatability and selectivity of the sensors were evaluated. By testing three consecutive sensing cycles, the response and recovery curves can be well repeated by the dynamic transient curve of a similar shape, demonstrating a fully reversible behavior at room temperature. The gas injection time and recovery time were kept constant following the protocol described in the previous section (dotted lines). The four different sensing materials react with different times with respect to the introduction of the vapors. Some of them had a quicker response, while others start sensing after a longer time with a sudden decrease of the electrical resistance due to different gas molecule−active surface interactions. Furthermore, long-term stability was tested, and there were no appreciable fluctuations regarding the baseline resistance and the sensing response over a 6 month time interval. More precisely, the electrical resistance slightly decreased with time in the range of 3−4%, while the sensing response has a deviation of less than 0.001%. It can be assumed that the good repeatability and stability are obtained through the stable 3D hierarchical architecture of the nanomaterial.

As a final step (Figure 11), the selectivity was studied. Except for the sensor based on ZnFe−Cl, it can be observed

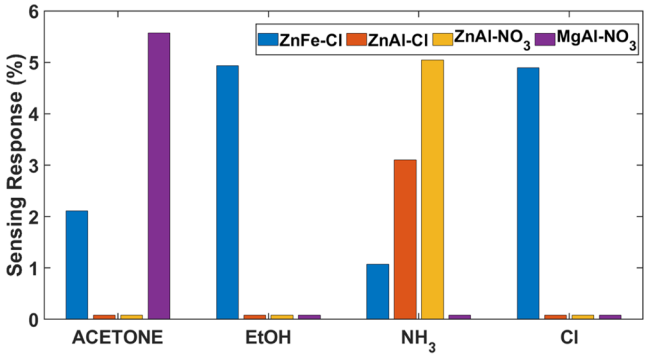

Figure 11. Sensing response of LDH gas sensors toward different analytes at a fixed concentration of 10% of saturated vapor at room temperature.

that all of the other electronic devices showed a remarkable selectivity at room temperature, being able to discriminate a unique analyte since the sensing response toward the other gases was almost zero. According to these excellent selectivity results achieved by some of these sensors, it was possible to discriminate NH_3 from acetone vapors by evaluating at the same time the responses of ZnAl−LDH (either intercalated with Cl or NO_3) and MgAl−NO_3-LDH, enhancing the cross-sensitivity.

By comparing the performance of the LDH-based sensors to that of the commercial one, it was observed that the latter obviously demonstrated higher sensitivity values than the former but comparable response times and even slower recovery times. This is a highly satisfying result since the LDH-based sensors operate at room temperature and do not require a heater element to support adsorption and desorption of the gas as the commercial sensor does. Table 3 summarizes all of the main results achieved for the tested gas chemiresistors.

Table 3. Best Performance Parameters Achieved for the Tested LDH Gas Sensors

parameters	sensor 1	sensor 2	sensor 3	sensor 4
LDH type	ZnFe−Cl	ZnAl−Cl	ZnAl−NO_3	MgAl−NO_3
selectivity	all analytes	NH_3	NH_3	acetone
sensing response (%)	4.9	3.8	5	5.6
response time (s)	188	216	235	137
recovery time (s)	137	243	221	194
limit of detection (LOD) (%)	2	2	6	6

As is well known, the transduction mechanism of the semiconductor gas sensor implies the adsorption of the analyte on the active sites of the material's surface with a consequent clear electrical resistance variation. However, it is difficult to have a clear understanding of the fine mechanism governing the interaction between the surface active sites of LDHs and the analyte. The most widely confirmed model was based on the modulation of the depletion layer by oxygen absorption.[44,53,54] Generally, in normal conditions, the oxygen in air diffuses inside the material and reacts on the surface of the material's grains. During these reactions, the oxygen turns into an anionic species, trapping free electrons from the LDH conduction band and ionizing themselves in $O^-_{2\ (ads)}$. The result is that the number of free carriers is modified by the environment that sets the resistance to the so-called baseline value. In this way, a hole accumulation layer is generated.[48,50,54] When the gas sensors are exposed to a reducing gas as all tested VOCs, the adsorbed oxygen will react with the analyte and the LDH surface. By freeing the trapped electrons back to the conduction band and neutralizing the hole carrier, the resistance will be reduced, while the conductivity is improved. The morphology, composition, and structure such as the porosity, grain size, specific surface area, and intercalation interspace are of paramount importance in relation to the sensing performance since they can affect the sensing mechanism. As it was possible to notice, changing the intercalation anion could lead to a better microstructure able to improve gas adsorption and diffusion. Therefore, more active sites made the absorption between oxygen species and the targeted gas easier. Lower gas responses were observed in samples with a molar ratio that was detrimental to the generation of a 3D flowerlike architecture, leading to a less porous structure that collapsed in some points, resulting in a smaller number of active sites for the gas molecules. When the morphology led to a well-ordered self-assembled multilamellar structure, even electron transport was enhanced and the transfer speed rate was increased from the inside to the outside. Similarly, the bridging effect due to the hydrogen bond between the surface hydroxyl groups and water molecules inside the interlayer efficiently improved the carriers' transport.[47,50]

https://doi.org/10.1021/acsomega.1c02038
ACS Omega 2021, 6, 20205−20217

3. EXPERIMENTAL

3.1. Materials. Acetone (ACS reagent grade, ≥99.5%), ethanol (EtOH) (analytical standard for GC, ≥99.9%), ammonium hydroxide solution ($NH_3{\cdot}H_2O$) (ACS reagent grade, 28.0−30.0 wt % NH_3 basis), magnesium nitrate hexahydrate [$Mg(NO_3)_2{\cdot}6H_2O$] (ACS reagent grade, ≥99.0%), zinc chloride hexahydrate [$ZnCl_2{\cdot}6H_2O$] (ACS reagent grade, ≥99.0%), zinc nitrate hexahydrate [$Zn(NO_3)_2{\cdot}6H_2O$] (ACS reagent grade, ≥99.0%), aluminum nitrate nonahydrate [$Al(NO_3)_3{\cdot}9H_2O$] (ACS reagent grade, ≥99.0%), aluminum chloride hydrate [$AlCl_3{\cdot}xH_2O$] (purity 99.999%), iron(III) chloride hexahydrate [$FeCl_3{\cdot}6H_2O$] (ACS reagent grade, ≥97.0%), and sodium hydroxide [NaOH] (ACS reagent grade, ≥97.0%) were purchased from Sigma-Aldrich (Milano, Italy). The common household bleach based on sodium hypochlorite (NaClO) (solution with 2.2 wt %) was employed. All of the chemicals were used as received without further purification. Si 4″ wafers finished with a 1 μm thick thermally grown SiO_2 layer were purchased from Si-Mat (Kaufering, Germany) and used as substrates for device fabrication.

3.2. LDH Synthesis. All LDH powders were prepared by the same constant pH coprecipitation method. Briefly, a sodium hydroxide solution about 2 M was added dropwise to a solution containing a suitable amount of the two specific soluble salts (Table 4) (divalent and trivalent metal cation sources) prepared in decarbonated distilled water until a pH of 10 was reached. The reaction pH was maintained constant at 10.00 by the continuous addition of NaOH solution and the temperature was kept at 70 °C maintaining a nitrogen atmosphere flow for 24 h. Only the LDH ZnFe−Cl was prepared at room temperature. The precipitates obtained were collected by centrifugation, washed several times in distilled water until neutral pH was reached, and dried under vacuum at 60 °C and stored.

Table 4. Different Salts (Divalent and Trivalent Metal Cation Sources) Used to Synthesize the Four Studied LDH Compositions

LDH composition	salts used	
ZnFe−Cl	$ZnCl_2{\cdot}6H_2O$ (0.075 M)	$FeCl_3{\cdot}6H_2O$ (0.025 M)
ZnAl−Cl $ZnCl_2$	$6H_2O$ (0.075 M)	$AlCl_3{\cdot}xH_2O$ (0.025 M)
ZnAl−NO_3	$Zn(NO_3)_2{\cdot}6H_2O$ (0.075 M)	$Al(NO_3)_3{\cdot}9H_2O$ (0.025 M)
MgAl−NO_3	$Mg(NO_3)_2{\cdot}6H_2O$ (0.075 M)	$Al(NO_3)_3{\cdot}9H_2O$ (0.025 M)

3.3. Substrate Preparation. The substrate was developed using standard cleanroom processes starting from 4″, single side polished, P type (100) Si wafers (resistivity 1−10 Ω·cm) finished with 1 μm thermal SiO_2. Contact pads and interdigitated electrodes (IDEs) were patterned by a liftoff process using a 7 μm layer of the AZ nLOF 2070 negative photoresist (MicroChemicals) deposited onto the Si wafer. A 10 nm thin layer of Ti was evaporated to promote the adhesion of the following 100 nm of Au that ensures the contact. The proposed design shown in Figure 1b consists of an 11 × 8 mm^2 area on top of which an array of IDEs composed of 100 fingers, characterized by a pitch of 44 μm was realized. Each finger was 9 mm long and 22 μm wide with a gap of 22 μm. The length and width of a single contact pad were 1.3 and 3.5 mm, respectively.

3.4. LDH Dispersion and Device Fabrication by Drop Casting. The typical formulation was prepared according to the specific LDH composition by dispersing the powder in different concentrations of ethanol to generate a stable suspension (Table 5). The dispersion underwent a sonication treatment by means of a Falc Labsonic LBS2 ultrasonic bath (Trevigliano, Italy), operating at room temperature for two consecutive cycles of 10 and 5 min each at 100% of the maximum power with a frequency of 59 kHz. This step enables a better dispersion of LDHs, allowing the employment of a drop-cast technique for the deposition of the sensing layer over the electrodes. Indeed, a micropipette was employed to drop 0.1 mL of each sonicated solution over the active area of the IDEs. To avoid the spreading of the solution over inactive areas, a PDMS mold was attached to the device and then removed after the deposition. At last, a short thermal treatment was performed by heating the samples at 65 °C for 10 min on a hotplate to speed up the evaporation of the solvent in excess. For each of the four LDH compositions, five sensors with the same geometry were fabricated.

Table 5. LDH Powder (10 mg) of the Four Analyzed Compositions Dispersed in Different Amounts of Ethanol

LDH composition	EtOH quantity (mL)
ZnFe−Cl	0.7
ZnAl−Cl	0.8
ZnAl−NO_3	0.9
MgAl−NO_3	0.6

3.5. Characterization. *3.5.1. Attenuated Total Reflectance−Fourier Transform Infrared Spectroscopy (ATR−FTIR).* FTIR analyses were performed in ATR mode to evaluate the chemical composition of the four LDH powders. The experiments were conducted on dried powder samples by means of a Thermo Scientific Nicolet iS50 FTIR Spectrometer (Milano, Italy) equipped with a single diamond crystal ATR accessory. The analysis was carried out with a resolution of 4 cm^{-1} and samples were scanned 32 times in the wavenumber range between 700 and 4000 cm^{-1}. A background measurement was performed on all samples prior to FTIR analysis. The results were acquired and processed using Omnic software.

3.5.2. Field Emission Scanning Electron Microscopy (FESEM) and Energy-Dispersive X-ray Analysis (EDX). The morphology and structure of the active films were investigated using a field emission scanning electron microscope (FESEM) Zeiss Supra 40 with the accelerating voltage of 3 kV. The same apparatus was used to perform an EDX analysis to provide a semiquantitative estimation of the elemental composition of the active layers and highlight their relative abundance.

3.5.3. X-ray Photoelectron Spectroscopy (XPS). X-ray photoelectron spectra (XPS) have been recorded with a Versa Probe PHI5000 using the monochromatic X-ray source Al Kα 1486.6 eV and pass energy of 187.85 eV for survey analysis to analyze the chemical state of elements and surface composition. O 1s high-resolution (HR) spectra were investigated and the peak was deconvoluted using Multipak Data Reduction Software. The binding energy scale was aligned fixing the C 1s peak at 284.80 eV and all of the HR peaks were fitted with mixed Gauss−Lorentzian line shapes (90% Gaussian) and the Shirley background.

3.5.4. X-ray Diffraction (XRD). X-ray diffraction patterns for all of the samples were obtained in the Bragg−Brentano

https://doi.org/10.1021/acsomega.1c02038
ACS Omega 2021, 6, 20205−20217

symmetric geometry using a PANalytical X'Pert Pro instrument (40 kV and 30 mA) equipped with an X'Celerator detector. Cu Kα monochromatic radiation was used as the X-ray source with λ = 1.54059 Å.

3.5.5. Sensing Setup. A dedicated measuring setup composed of a detection chamber connected to an Environics gas mixing system (series 4000) able to control the selected concentrations of the solvent vapors to the samples was employed to acquire the LDHs' dynamic sensing responses.

In more detail, a stream of oil-free dry air (DA) is exploited both as the carrier and diluting gas. As it enters the gas mixing system, the main stream is separated into two fluxes and regulated by means of two mass flow controllers (MFC). The DA flows through a bubbler properly filled with the volatile organic compound (VOC) to be tested, producing its saturated vapor. Then, the two flows are recombined, mixed, and directed to a detection chamber made of a stainless-steel assembly with a 100 mm inner diameter where two samples could be housed at the same time. There exists a latency period from the opening time of the valve and the moment in which the vapor fills the chamber and can be detected. This delay affects the response and recovery time in the same way. The operational temperature for the sensing measurements herein reported is 21 °C and it was measured with a PT1000 sensor. A Figaro TGS2600 sensor placed inside the chamber is used as a reference. All of the gas tests in this work were carried out by setting a constant flow of dry air at 100 sccm and by varying the concentration of the diluted gases from 1 to 10% (1−10 sccm). The sensing response was evaluated toward four different gases exploiting the following liquid analytes: acetone, EtOH, NaClO solution (testing chlorine-based vapor), and NH_4OH solution (testing NH_3 vapor).

3.5.6. Sensing Analyses. The electrical resistance was investigated using two-probe measurements, exploiting a data acquisition unit 34970A supplied by Keysight (Milano, Italy). In the DC analysis, a voltage was applied between the electrodes and the current was measured, directly acquiring the resistance as a function of time. For each test, dry air was introduced for 40 s to get the baseline. Successively, the sensor was exposed to the analyte at the desired concentration for 240 s, followed by further 360 s that was set as the recovery time. Even though a saturated response is not reached, the same procedure was always applied to make measurements comparable and the variation of electrical resistance was always clearly visible. Between successive measurements, to avoid the influence of contamination coming from previous tests or when changing the analytes, the chamber lid was opened and dry air was fluxed for a few minutes.

The typical sensing response of the device to a particular gas (S) is calculated as the ratio between the steady-state resistance variation ΔR and the baseline resistance of the device (eq 2)

$$S = \frac{\Delta R}{R_{\text{baseline}}} \tag{2}$$

In this work, the formula used is reported below (eq 3)

$$S\% = \left(1 - \frac{R_{\text{baseline}}}{R_{\text{gas}}}\right) \times 100 \tag{3}$$

Saturated vapors of the VOCs were extracted by bubbling dry air through the bubbler. The concentration of the VOC vapor is expressed as a percentage obtained from the ratio between the saturated vapor flow coming out of the bubbler and divided by the total flow reaching the detection chamber, using the following equation (eq 4)

$$C(\text{saturated vapor }\%) = \left(\frac{P^*}{P} \times \frac{f}{f+F}\right) \times 100 \tag{4}$$

where P is the input air pressure (atmospheric pressure in this case), P^* is the saturated partial pressure of the analyte, and f and F are the mass flow rates of MFC of the pure dry air and MFC of the carrier, respectively. P^* is calculated by Antoine's equation (eq 5) as a function of temperature and Antoine's component-specific constants A, B, and C.[55−58]

$$P^* = 10^{(A-B/C+T)} \tag{5}$$

At room temperature the saturated vapor pressures of acetone, ethanol, NaClO, and NH_3 are 0.254, 0.061, 0.020, and 0.732 atm, respectively. Furthermore, the response time (t_{res}) is defined as the time required for the saturation value to reach 90% of the total resistance change, whereas the recovery time (t_{rec}) is the reverse of the response time related to the desorption of the gas. Additionally, the limit of detection (LOD) is identified as the lowest quantity of analyte that can be distinguished from the absence of that vapor. This value is strictly related to the sensitivity parameter because the greater the response of the sensor, the easier the possibility of detecting a small fraction of a particular vapor.

4. CONCLUSIONS

In this work, layered double hydroxides were successfully synthesized via a coprecipitation method, and gas sensors were fabricated through cleanroom technologies and drop casting employing LDHs as the sensing element and demonstrating a wide range of potentialities to be explored. They manage to properly operate at room temperature, without the need of a heating element, which represents a clear advantage from the point of view of power consumption. The gas sensing tests showed that all of the LDH-based sensors were correctly able to reversibly detect acetone, ethanol, NH_3, and chlorine vapors at room temperature, reaching sensing response values up to 6%, comparable to many results reported in the literature.[17,18,42,43,54] Moreover, a simple variation of the chemical composition of the material could act on the sensitivity and selectivity of the sensor, helping the discrimination of different analytes. Furthermore, the excellent gas-sensing performance at room temperature can be related to the unique morphology of the material, characterized by a 3D hierarchical flowerlike architecture with a high porosity, which provides several diffusion channels, allowing a fast diffusion of the gas, and it enhances the number of active sites for the absorption both on the surface and inside the bulk of the material.

The future perspectives are the fabrication of sensor arrays based on different LDHs obtained by changing the specific chemical structure to tune the response, namely, a simple and selective electronic nose prototype, able to perform room temperature detection of an increasing number of specific gases at very low concentrations using the same low-cost and low working temperature material.

■ ASSOCIATED CONTENT

Supporting Information

The Supporting Information is available free of charge at https://pubs.acs.org/doi/10.1021/acsomega.1c02038.

https://doi.org/10.1021/acsomega.1c02038
ACS Omega 2021, 6, 20205−20217

Additional FESEM characterization at different magnifications for all of the compositions (Figures S1 and S2) (PDF)

AUTHOR INFORMATION

Corresponding Author

Simone Luigi Marasso − *Dipartimento di Scienza Applicata e Tecnologia (DISAT), Politecnico di Torino, 10129 Torino, Italy; CNR-IMEM, 43124 Parma, Italy;* orcid.org/0000-0003-4570-2674; Email: simone.marasso@polito.it

Authors

Lorenzo Vigna − *Dipartimento di Scienza Applicata e Tecnologia (DISAT), Politecnico di Torino, 10129 Torino, Italy;* orcid.org/0000-0002-2492-0675

Arianna Nigro − *Dipartimento di Scienza Applicata e Tecnologia (DISAT), Politecnico di Torino, 10129 Torino, Italy;* Present Address: Departement Physik, Universität Basel, Klingelbergstrasse 82, 4056 Basel, Switzerland

Alessio Verna − *Dipartimento di Scienza Applicata e Tecnologia (DISAT), Politecnico di Torino, 10129 Torino, Italy*

Ivan Vito Ferrari − *Center for Sustainable Future Technologies, Istituto Italiano di Tecnologia, 10144 Torino, Italy*

Sergio Bocchini − *Center for Sustainable Future Technologies, Istituto Italiano di Tecnologia, 10144 Torino, Italy;* orcid.org/0000-0003-2876-2317

Marco Fontana − *Center for Sustainable Future Technologies, Istituto Italiano di Tecnologia, 10144 Torino, Italy*

Angelica Chiodoni − *Center for Sustainable Future Technologies, Istituto Italiano di Tecnologia, 10144 Torino, Italy*

Candido Fabrizio Pirri − *Dipartimento di Scienza Applicata e Tecnologia (DISAT), Politecnico di Torino, 10129 Torino, Italy; Center for Sustainable Future Technologies, Istituto Italiano di Tecnologia, 10144 Torino, Italy*

Matteo Cocuzza − *Dipartimento di Scienza Applicata e Tecnologia (DISAT), Politecnico di Torino, 10129 Torino, Italy; CNR-IMEM, 43124 Parma, Italy;* orcid.org/0000-0002-3506-216X

Complete contact information is available at: https://pubs.acs.org/10.1021/acsomega.1c02038

Author Contributions

M.C., S.L.M., A.V., and L.V. conceptualization; L.V. and A.N. data curation; L.V., A.N., and I.V.F. formal analysis; C.F.P. funding acquisition; L.V., A.N., and M.F. investigation; S.L.M. methodology; S.L.M., M.C., A.V., and L.V. supervision; L.V. and M.F. validation; L.V. and A.N. visualization; L.V. and A.N. writing—original draft; L.V., A.N., M.F., S.B., A.C., S.L.M., M.C., and A.V. writing—review and editing.

Notes

The authors declare no competing financial interest.

ACKNOWLEDGMENTS

The authors thank Alberto Ballesio (FESEM analysis), Camilla Noè (FTIR analysis), and Matteo Parmeggiani (XPS data analysis) for their help.

REFERENCES

(1) Hochstetter, C. Untersuchung Über Die Zusammensetzung Einiger Mineralien. *J. Prakt. Chem.* **1842**, *27*, 375−378.

(2) Feitknecht, W.; Gerber, M. Acknowledgement of the Double Hydroxide and Base Double Salt III Manesium-Aluminium Double Hydroxide. *Helv. Chim. Acta* **1942**, *27*, 131−137.

(3) Mochane, M. J.; Magagula, S. I.; Sefadi, J. S.; Sadiku, E. R.; Mokhena, T. C. Morphology, Thermal Stability, and Flammability Properties of Polymer-Layered Double Hydroxide (Ldh) Nanocomposites: A Review. *Crystals* **2020**, *10*, No. 612.

(4) Prestopino, G.; Arrabito, G. Layered Double Hydroxides. *Crystals* **2020**, *10*, No. 1050.

(5) Arrabito, G.; Bonasera, A.; Prestopino, G.; Orsini, A.; Mattoccia, A.; Martinelli, E.; Pignataro, B.; Medaglia, P. G. Layered Double Hydroxides: A Toolbox for Chemistry and Biology. *Crystals* **2019**, *9*, No. 361.

(6) Bravo-Suárez, J. J.; Páez-Mozo, E. A.; Oyama, S. T. Review of the Synthesis of Layered Double Hydroxides: A Thermodynamic Approach. *Quim. Nova* **2004**, *27*, 601−604.

(7) Feitknecht, W.; Gerber, M. Zur Kenntnis Der Doppelhydroxyde Und Basischen Doppelsalze II. Über Mischfällungen Aus Calcium-Aluminiumsalzlösungen. *Helv. Chim. Acta* **1942**, *25*, 106−131.

(8) Hu, G.; Wang, N.; O'Hare, D.; Davis, J. One-Step Synthesis and AFM Imaging of Hydrophobic LDH Monolayers. *Chem. Commun.* **2006**, *12*, 287−289.

(9) Liu, A.; Dahn, J. R. The Formation of Layered Double Hydroxide Phases in the Coprecipitation Syntheses of [Ni0.80 Co0.15](1−x)/0.95 Alx (OH)2 (AnionN−)x/n (x = 0−0.2, n = 1, 2). *ChemEngineering* **2019**, *3*, No. 38.

(10) Bergaya, F.; Theng, B. K. G.; Lagaly, G. *Handbook of Clay Science*, 1st ed.; Elsevier, 2006.

(11) Polese, D.; Mattoccia, A.; Giorgi, F.; Pazzini, L.; Di Giamberardino, L.; Fortunato, G.; Medaglia, P. G. A Phenomenological Investigation on Chlorine Intercalated Layered Double Hydroxides Used as Room Temperature Gas Sensors. *J. Alloys Compd.* **2017**, *692*, 915−922.

(12) Polese, D.; Mattoccia, A.; Cavaiola, C.; Zoppi, J.; Pazzini, L.; Fortunato, G.; Medaglia, P. G.; Maiolo, L. AC Characterization of Nitrate Intercalated Layered Double Hydroxides Gas Sensors, *Proceedings of IEEE Sensors*, 2017; pp 1−3.

(13) Polese, D.; Mattoccia, A.; Giorgi, F.; Pazzini, L.; Ferrone, A.; Di Giamberardino, L.; Maiolo, L.; Pecora, A.; Convertino, A.; Fortunato, G.; Medaglia, P. G. Layered Double Hydroxides Intercalated with Chlorine Used as Low Temperature Gas Sensors. *Procedia Eng.* **2015**, *120*, 1175−1178.

(14) Tang, S.; Yao, Y.; Chen, T.; Kong, D.; Shen, W.; Lee, H. K. Recent Advances in the Application of Layered Double Hydroxides in Analytical Chemistry: A Review. *Anal. Chim. Acta* **2020**, *1103*, 32−48.

(15) Kang, G.; Zhu, Z.; Tang, B. H.; Wu, C. H.; Wu, R. J. Rapid Detection of Ozone in the Parts per Billion Range Using a Novel Ni−Al Layered Double Hydroxide. *Sens. Actuators, B* **2017**, *241*, 1203−1209.

(16) Qin, Y.; Wang, L.; Wang, X. A High Performance Sensor Based on PANI/ZnTi-LDHs Nanocomposite for Trace NH3 Detection. *Org. Electron.* **2019**, *66*, 102−109.

(17) Qin, Y.; Wang, X.; Wang, L. Hierarchical In(OH)3/ZnAlIn-LDHs Nanocomposite with Extremely Low Detection Limit for NO2 Sensing. *J. Mater. Sci. Mater. Electron.* **2019**, *30*, 19552−19560.

(18) He, L.; Zhang, W.; Zhang, X.; Bai, X.; Chen, J.; Ikram, M.; Zhang, G.; Shi, K. 3D Flower-like NiCo-LDH Composites for a High-Performance NO2 Gas Sensor at Room Temperature. *Colloids Surf., A* **2020**, *603*, No. 125142.

(19) Zhao, M.; Zhao, Q.; Li, B.; Xue, H.; Pang, H.; Chen, C. Recent Progress in Layered Double Hydroxide Based Materials for Electrochemical Capacitors: Design, Synthesis and Performance. *Nanoscale* **2017**, *9*, 15206−15225.

(20) Mishra, G.; Dash, B.; Pandey, S. Layered Double Hydroxides: A Brief Review from Fundamentals to Application as Evolving Biomaterials. *Appl. Clay Sci.* **2018**, *153*, 172−186.

(21) Chatterjee, A.; Bharadiya, P.; Hansora, D. Layered Double Hydroxide Based Bionanocomposites. *Appl. Clay Sci.* **2019**, *177*, 19−36.
(22) Khan, S. B.; Liu, C.; Jang, E. S.; Akhtar, K.; Han, H. Encapsulation of Organic UV Ray Absorbents into Layered Double Hydroxide for Photochemical Properties. *Mater. Lett.* **2011**, *65*, 2923−2926.
(23) He, S.; An, Z.; Wei, M.; Evans, D. G.; Duan, X. Layered Double Hydroxide-Based Catalysts: Nanostructure Design and Catalytic Performance. *Chem. Commun.* **2013**, *49*, 5912−5920.
(24) Li, C.; Wei, M.; Evans, D. G.; Duan, X. Layered Double Hydroxide-Based Nanomaterials as Highly Efficient Catalysts and Adsorbents. *Small* **2014**, *10*, 4469−4486.
(25) Ryu, S. J.; Jung, H.; Oh, J. M.; Lee, J. K.; Choy, J. H. Layered Double Hydroxide as Novel Antibacterial Drug Delivery System. *J. Phys. Chem. Solids* **2010**, *71*, 685−688.
(26) Bi, X.; Zhang, H.; Dou, L. Layered Double Hydroxide-Based Nanocarriers for Drug Delivery. *Pharmaceutics* **2014**, *6*, 298−332.
(27) Choy, J. H.; Jung, J. S.; Oh, J. M.; Park, M.; Jeong, J.; Kang, Y. K.; Han, O. J. Layered Double Hydroxide as an Efficient Drug Reservoir for Folate Derivatives. *Biomaterials* **2004**, *25*, 3059−3064.
(28) Jin, S.; Fallgren, P. H.; Morris, J. M.; Chen, Q. Removal of Bacteria and Viruses from Waters Using Layered Double Hydroxide Nanocomposites. *Sci. Technol. Adv. Mater.* **2007**, *8*, 67−70.
(29) Maiolo, L.; Pecora, A.; Polese, D.; Pazzini, L.; Ferrone, A.; Mattoccia, A.; Medaglia, P. Low Working Temperature Operation of Layered Double Hydroxides Sensors for Air Quality Monitoring in Smart Cities, *2016 IEEE 25th International Symposium on Industrial Electronics (ISIE)*, 2016; pp 986−990.
(30) Zhang, L.; Tian, F.; Nie, H.; Dang, L.; Li, G.; Ye, Q.; Kadri, C. Classification of Multiple Indoor Air Contaminants by an Electronic Nose and a Hybrid Support Vector Machine. *Sens. Actuators, B* **2012**, *174*, 114−125.
(31) Schütze, A.; Baur, T.; Leidinger, M.; Reimringer, W.; Jung, R.; Conrad, T.; Sauerwald, T. Highly Sensitive and Selective VOC Sensor Systems Based on Semiconductor Gas Sensors: How To? *Environ.* **2017**, *4*, No. 20.
(32) Jaiswal, A.; Gautam, R. K.; Chattopadhyaya, M. C. Layered Double Hydroxides and the Environment: An Overview. *Adv. Mater. Agric. Food Environ. Saf.* **2014**, 1−26.
(33) Vigna, L.; Verna, A.; Marasso, S. L.; Sangermano, M.; D'Angelo, P.; Pirri, F. C.; Cocuzza, M. The effects of secondary doping on ink-jet printed PEDOT:PSS gas sensors for VOCs and NO_2 detection. *Sens. Actuators, B* **2021**, *345*, 130381.
(34) Razza, N.; Blanchet, B.; Lamberti, A.; Pirri, F. C.; Tulliani, J. M.; Bozano, L. D.; Sangermano, M. UV-Printable and Flexible Humidity Sensors Based on Conducting/Insulating Semi-Interpenetrated Polymer Networks. *Macromol. Mater. Eng.* **2017**, *302*, No. 1700161.
(35) Bai, H.; Shi, G. Gas Sensors Based on Conducting Polymers. *Sensors* **2007**, 267−307.
(36) Scordo, G.; Bertana, V.; Ballesio, A.; Carcione, R.; Marasso, S. L.; Cocuzza, M.; Pirri, C. F.; Manachino, M.; Gomez, M. G.; Vitale, A.; Chiodoni, A.; Tamburri, E.; Scaltrito, L. Effect of Volatile Organic Compounds Adsorption on 3D-Printed Pegda:Pedot for Long-Term Monitoring Devices. *Nanomaterials* **2021**, *11*, No. 94.
(37) Morandi, S.; Prinetto, F.; Di Martino, M.; Ghiotti, G.; Lorret, O.; Tichit, D.; Malagù, C.; Vendemiati, B.; Carotta, M. C. Synthesis and Characterisation of Gas Sensor Materials Obtained from Pt/Zn/Al Layered Double Hydroxides. *Sens. Actuators, B* **2006**, *118*, 215−220.
(38) Fine, G. F.; Cavanagh, L. M.; Afonja, A.; Binions, R. Metal Oxide Semi-Conductor Gas Sensors in Environmental Monitoring. *Sensors* **2010**, *10*, 5469−5502.
(39) Marasso, S. L.; Tommasi, A.; Perrone, D.; Cocuzza, M.; Mosca, R.; Villani, M.; Zappettini, A.; Calestani, D. A New Method to Integrate ZnO Nano-Tetrapods on MEMS Micro-Hotplates for Large Scale Gas Sensor Production. *Nanotechnology* **2016**, *27*, No. 385503.
(40) Xu, D. M.; Guan, M. Y.; Xu, Q. H.; Guo, Y. Multilayer Films of Layered Double Hydroxide/Polyaniline and Their Ammonia Sensing Behavior. *J. Hazard. Mater.* **2013**, *262*, 64−70.
(41) Vigna, L.; Fasoli, A.; Cocuzza, M.; Pirri, F. C.; Bozano, L. D.; Sangermano, M. A Flexible, Highly Sensitive, and Selective Chemiresistive Gas Sensor Obtained by In Situ Photopolymerization of an Acrylic Resin in the Presence of MWCNTs. *Macromol. Mater. Eng.* **2018**, *1800453*, No. 1800453.
(42) Qin, Y.; Zhao, R.; Bai, C. Layered Double Hydroxide-Oriented Assembly by Negatively Charged Graphene Oxide for NO2 Sensing at Ppb Level. *New J. Chem.* **2020**, *44*, 16985−16994.
(43) Zhang, X.; Ikram, M.; Liu, Z.; Teng, L.; Xue, J.; Wang, D.; Li, L.; Shi, K. Expanded Graphite/NiAl Layered Double Hydroxide Nanowires for Ultra-Sensitive, Ultra-Low Detection Limits and Selective NOx Gas Detection at Room Temperature. *RSC Adv.* **2019**, *9*, 8768−8777.
(44) Liu, Z.; Teng, L.; Ma, L.; Liu, Y.; Zhang, X.; Xue, J.; Ikram, M.; Ullah, M.; Li, L.; Shi, K. Porous 3D Flower-like CoAl-LDH Nanocomposite with Excellent Performance for NO2 Detection at Room Temperature. *RSC Adv.* **2019**, *9*, 21911−21921.
(45) Qin, Y.; Wang, L.; Wang, X. Hierarchical Layered Double Hydroxides with Ag Nanoparticle Modification for Ethanol Sensing. *Nanotechnology* **2018**, *29*, No. 275502.
(46) Li, Y.; Zhou, F.; Gao, L.; Duan, G. Co3O4 Nanosheet-Built Hollow Spheres Containing Ultrafine Neck-Connected Grains Templated by PS@Co-LDH and Their Ppb-Level Gas-Sensing Performance. *Sens. Actuators, B* **2018**, *261*, 553−565.
(47) Hong, D.; Zhang, J.; Rehman, A. U.; Gong, L.; Zhou, J.; Kan, K.; Li, L.; Shi, K. One-Step Synthesis of Hierarchical Ni-Fe-Al Layered Double Hydroxide with Excellent Sensing Properties for NOx at Room Temperature. *RSC Adv.* **2016**, *6*, 103192−103198.
(48) Xu, Q. H.; Xu, D. M.; Guan, M. Y.; Guo, Y.; Qi, Q.; Li, G. D. ZnO/Al2O3/CeO2 Composite with Enhanced Gas Sensing Performance. *Sens. Actuators, B* **2013**, *177*, 1134−1141.
(49) Tommasi, A.; Cocuzza, M.; Perrone, D.; Pirri, C.; Mosca, R.; Villani, M.; Delmonte, N.; Zappettini, A.; Calestani, D.; Marasso, S. Modeling, Fabrication and Testing of a Customizable Micromachined Hotplate for Sensor Applications. *Sensors* **2017**, *17*, 62.
(50) Ge, Y.; Kan, K.; Yang, Y.; Zhou, L.; Jing, L.; Shen, P.; Li, L.; Shi, K. Highly Mesoporous Hierarchical Nickel and Cobalt Double Hydroxide Composite: Fabrication, Characterization and Ultrafast NOx Gas Sensors at Room Temperature. *J. Mater. Chem. A* **2014**, *2*, 4961−4969.
(51) Sun, H.; Chu, Z.; Hong, D.; Zhang, G.; Xie, Y.; Li, L.; Shi, K. Three-Dimensional Hierarchical Flower-like Mg-Al-Layered Double Hydroxides: Fabrication, Characterization and Enhanced Sensing Properties to NOx at Room Temperature. *J. Alloys Compd.* **2016**, *658*, 561−568.
(52) Wang, H.; Gao, J.; Li, Z.; Ge, Y.; Kan, K.; Shi, K. One-Step Synthesis of Hierarchical α-Ni(OH)2 Flowerlike Architectures and Their Gas Sensing Properties for NOx at Room Temperature. *CrystEngComm* **2012**, *14*, 6843−6852.
(53) Wang, J.; Wang, L.; Gao, J.; Zhou, L.; Ge, Y.; Jing, L.; Shi, K.; Li, L. Detection of NOx down to Ppb Levels at Room Temperature Based on Highly Mesoporous Hierarchical Ni(OH)2−In(OH)3 Double Hydroxide Composites. *J. Mater. Sci. Mater. Electron.* **2015**, *26*, 6612−6624.
(54) Hong, Y.; Wang, D.; Lin, C.; Luo, S.; Pan, Q.; Li, L.; Shi, K. Room-Temperature Efficient NO2 Gas Sensors Fabricated by Porous 3D Flower-like ZnAl-Layered Double Hydroxides. *New J. Chem.* **2020**, *44*, 18469−18480.
(55) Dean, J. A. *Lange'S Handbook of Chemistry*, 15th ed.; McGraw-Hill: New York, 1999; Vol. *5*.
(56) Araujo-Lopez, E.; Lopez-Echeverry, J. S.; Reif-Acherman, S. The Antoine Equation of State: Rediscovering the Potential of an Almost Forgotten Expression for Calculating Volumetric Properties of Pure Compounds. *Chem. Eng. Sci.* **2018**, *177*, 89−109.

https://doi.org/10.1021/acsomega.1c02038
ACS Omega 2021, 6, 20205−20217

(57) Kar, P.; Pradhan, N. C.; Adhikari, B. Application of Sulfuric Acid Doped Poly (m-Aminophenol) as Aliphatic Alcohol Vapor Sensor Material. *Sens. Actuators, B* **2009**, *140*, 525−531.
(58) Badhulika, S.; Myung, N. V.; Mulchandani, A. Conducting Polymer Coated Single-Walled Carbon Nanotube Gas Sensors for the Detection of Volatile Organic Compounds. *Talanta* **2014**, *123*, 109−114.
(59) Conterosito, E.; Palin, L.; Antonioli, D.; Viterbo, D.; Mugnaioli, E.; Kolb, U.; Perioli, L.; Milanesio, M.; Gianotti, V. Structural Characterisation of Complex Layered Double Hydroxides and TGA-GC-MS Study on Thermal Response and Carbonate Contamination in Nitrate- and Organic-Exchanged Hydrotalcites. *Chem. - Eur. J.* **2015**, *21*, 14975−14986.
(60) Iuzviuk, M. H.; Bouali, A. C.; Serdechnova, M.; Yasakau, K. A.; Wieland, D. C. F.; Dovzhenko, G.; Mikhailau, A.; Blawert, C.; Zobkalo, I. A.; Ferreira, M. G. S.; Zheludkevich, M. L. In Situ Kinetics Studies of Zn-Al LDH Intercalation with Corrosion Related Species. *Phys. Chem. Chem. Phys.* **2020**, *22*, 17574−17586.
(61) Richetta, M.; Digiamberardino, L.; Mattoccia, A.; Medaglia, P. G.; Montanari, R.; Pizzoferrato, R.; Scarpellini, D.; Varone, A.; Kaciulis, S.; Mezzi, A.; Soltani, P.; Orsini, A. Surface Spectroscopy and Structural Analysis of Nanostructured Multifunctional (Zn, Al) Layered Double Hydroxides. *Surf. Interface Anal.* **2016**, *48*, 514−518.
(62) Parida, K. M.; Mohapatra, L. Carbonate Intercalated Zn/Fe Layered Double Hydroxide: A Novel Photocatalyst for the Enhanced Photo Degradation of Azo Dyes. *Chem. Eng. J.* **2012**, *179*, 131−139.

https://doi.org/10.1021/acsomega.1c02038
ACS Omega 2021, 6, 20205−20217